Inorganic Chemistry

pubs.acs.org/IC Article

A Water Molecule Residing in the $Fe_{a3}^{3+}\cdots Cu_B^{2+}$ Dinuclear Center of the Resting Oxidized as-Isolated Cytochrome *c* Oxidase: A Density Functional Study

Wen-Ge Han Du, Duncan McRee, Andreas W. Götz, and Louis Noodleman*

Cite This: *Inorg. Chem.* 2020, 59, 8906–8915 Read Online

ACCESS | Metrics & More | Article Recommendations | Supporting Information

ABSTRACT: Although the dinuclear center (DNC) of the resting oxidized "as-isolated" cytochrome *c* oxidase (C*c*O) is not a catalytically active state, its detailed structure, especially the nature of the bridging species between the Fe_{a3}^{3+} and Cu_B^{2+} metal sites, is still both relevant and unsolved. Recent crystallographic work has shown an extended electron density for a peroxide type dioxygen species (O1−O2) bridging the Fe_{a3} and Cu_B centers. In this paper, our density functional theory (DFT) calculations show that the observed peroxide type electron density between the two metal centers is most likely a mistaken analysis due to overlap of the electron density of a water molecule located at different positions between apparent O1 and O2 sites in DNCs of different C*c*O molecules with almost the same energy. Because the diffraction pattern and the resulting electron density map represent the effective long-range order averaged over many molecules and unit cells in the X-ray structure, this averaging can lead to an apparent observed superposition of different water positions between the Fe_{a3}^{3+} and Cu_B^{2+} metal sites.

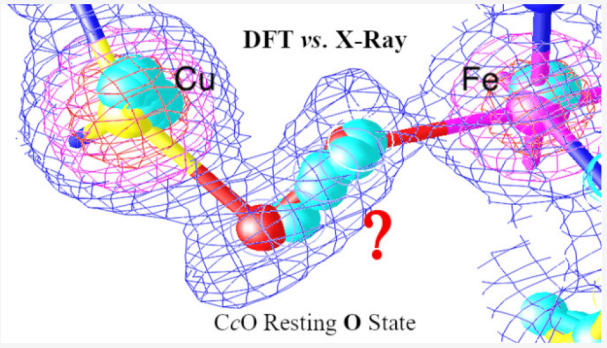

1. INTRODUCTION

Cytochrome *c* oxidase (C*c*O), located in the inner mitochondrial or bacterial membrane, is the terminal enzyme in the respiratory chain that reduces O_2 to H_2O and pumps protons across the membrane to create the chemiosmotic proton gradient used by ATP synthase to synthesize ATP.[1−5] The catalytic site of C*c*O that binds and reduces O_2 by $4e^-/4H^+$ transfer contains a heme a_3 (Fe_{a3}) and a Cu (Cu_B) ion. Fe_{a3} and Cu_B are close to each other (~5 Å). This Fe_{a3}-Cu_B active site is usually called the dinuclear (or binuclear) center/complex (DNC or BNC). In all types of C*c*O molecules, the iron in the Fe_{a3} site is coordinated to heme and an axial histidine ligand (His384; residue numbers in this paper are by default for ba_3 C*c*O from *Thermus thermophilus* (*Tt*)), while the copper in the Cu_B site is coordinated to three histidine ligands: His233, His282, and His283. His233 covalently links to the Tyr237 side chain. This unique cross-linked tyrosine residue takes an important role in the processes of electron/proton transfer in C*c*O. There are two other redox centers also present in C*c*O. One is a homodinuclear Cu dimer ($2Cu_A$), which serves as the initial site of electron entry to C*c*O,[6,7] and the other is also a heme, which is heme A (Fe_a) in the case of the aa_3 type of C*c*O or heme B (Fe_b) in the ba_3 type of C*c*O. Electrons transfer from cytochrome *c* to Cu_A, then on to heme A/B, and from there to the DNC Fe_{a3}-Cu_B.[8,9] The DNC structures of aa_3 and ba_3 oxidases are nearly identical.

The oxidation, spin, and ligation states of the Fe_{a3} and Cu_B sites change during the catalytic cycle. Starting from the binding of O_2 with the reduced (**R**) DNC, several catalytic intermediates (see Figure 1) have been well characterized by resonance Raman (rR) studies.[10−14] Very recently, we have calculated the Fe_{a3}−O/O−O stretching frequencies for several DNC intermediate states and compared them with the available rR data.[15] When molecular O_2 binds with Fe_{a3}^{2+}, state $\mathbf{A}[Fe_{a3}^{3+}-O_2^{\bullet-}\cdots Cu_B^{+}]$ is formed,[10−14,16,17] where $Fe_{a3}^{3+}-O_2^{\bullet-}$ is likely in a similar bent end-on geometry as in oxymyoglobin.[15,18−20] The following characterized states are **P**, **F**, and $\mathbf{O}_H$. State **P** is not a peroxide-containing compound (as implied in the notation), but one in which the dioxygen O−O bond has already been cleaved.[21−25] It can be represented as $\mathbf{P}[Fe_{a3}^{4+}{=}O^{2-}\cdots OH^{-}-Cu_B^{2+}]$. State $\mathbf{F}[Fe_{a3}^{4+}{=}O^{2-}\cdots H_2O-Cu_B^{2+}]$ is then formed when the OH^- ligand of Cu_B^{2+} in **P** receives a proton and becomes a water ligand. Our density functional calculations reproduced the rR observed ~20 cm^{-1} shift of the Fe_{a3}−O stretching mode from state $\mathbf{P}[Fe_{a3}^{4+}{=}O^{2-}\cdots OH^{-}-Cu_B^{2+}]$ to $\mathbf{F}[Fe_{a3}^{4+}{=}O^{2-}\cdots H_2O-Cu_B^{2+}]$.[15] Therefore, it is

Received: March 9, 2020
Published: June 11, 2020

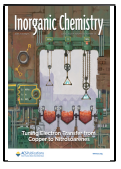

https://dx.doi.org/10.1021/acs.inorgchem.0c00724
Inorg. Chem. 2020, 59, 8906−8915

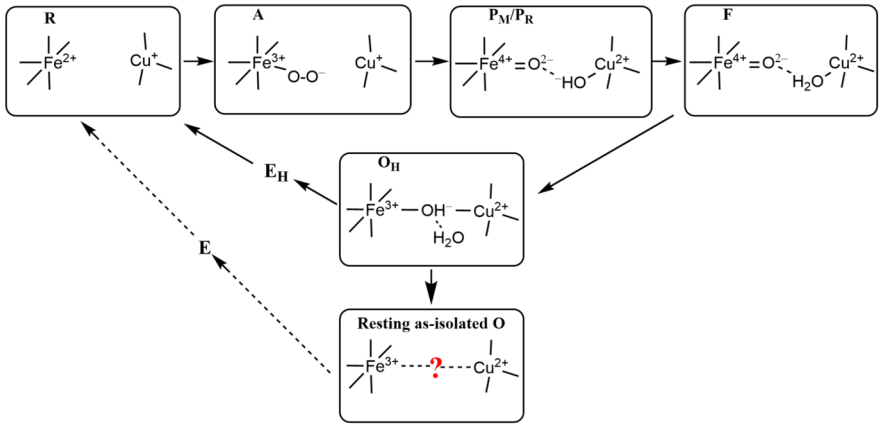

Figure 1. A, **P**, **F**, and $\mathbf{O_H}$ are the catalytic intermediates that are identified by resonance Raman (rR) experiments after O_2 binding with Fe_{a3}^{2+} in the reduced (**R**) state. Their DNCs are likely in the forms presented above. However, the resting "as-isolated" oxidized **O** state is different from the active $\mathbf{O_H}$ state.

highly likely that the H_2O ligand is still on the Cu_B^{2+} site in state **F**. On the basis of our energy calculations,[26] an $\mathbf{F_H}[Fe_{a3}^{4+}{=}O^{2-}{\cdots}Cu_B^{2+}]$ state, where the H_2O ligand has dissociated from the Cu_B^{2+} site and the O^{2-} on Fe_{a3}^{4+} also weakly binds with Cu_B^{2+}, although not observed, may exist before the catalytically active form of the oxidized state $\mathbf{O_H}$ is formed by $1e^-/1H^+$ reduction of $Fe_{a3}^{4+}{=}O^{2-}$ to $Fe_{a3}^{3+}{-}OH^-$. A very low frequency $Fe_{a3}^{3+}{-}OH^-$ stretching mode at 450 cm^{-1} was observed in $\mathbf{O_H}$, and our calculations have shown that this low Fe−O stretching mode can be produced by a nearly symmetrically bridged $\mathbf{O_H}[Fe_{a3}^{3+}{-}OH^-{-}Cu_B^{2+}]$ structure with a relatively long Fe_{a3}−O distance near 2 Å.[15]

It is interesting to note that the DNC structure of the resting "as-isolated" oxidized (**O**) state is different from that of the active $\mathbf{O_H}$ state. $\mathbf{O_H}$ is a metastable catalytically active state, which decays to the relaxed lower-energy **O** state when a one-electron ($1e^-$) transfer to the DNC in $\mathbf{O_H}$ is delayed (or absent) during redox cycling, just after cycling from $\mathbf{R} \rightarrow \mathbf{O_H}$. Given sufficient time, $\mathbf{O_H}$ decays to **O**, which is the same as the isolated oxidized ("resting") state. The differences between **O** and $\mathbf{O_H}$ were first seen in kinetics studies using optical difference spectroscopy and electrometry to examine the $1e^-$ redox transitions $\mathbf{O_H} + 1e^- \rightarrow \mathbf{E_H}$ in comparison to $\mathbf{O} + 1e^- \rightarrow \mathbf{E}$.[9,27] In the next step to regenerate **R**, one more electron is added to the active site, and a proton may move into the active site region to protonate an OH^- (if needed). The observed kinetics of $\mathbf{O_H} \rightarrow \mathbf{E_H}$ is very different from that of $\mathbf{O} \rightarrow \mathbf{E}$, and the first gives more efficient electron transfer, ending at Cu_B, and more effective proton transfer, for both ba_3 and aa_3 type enzymes. In the kinetic experiments, to generate state $\mathbf{E_H}$ from $\mathbf{O_H}$, the $1e^-$ added is injected after a timed laser flash, and the prior reaction cycle ending in state $\mathbf{O_H}$ is also started by a laser flash in the CO-inhibited **R** state,[28] synchronized with a pulse of molecular oxygen.[27] Overall, the full $2e^-$ reduction of $\mathbf{O} \rightarrow \mathbf{R}$ is much slower than that of $\mathbf{O_H} \rightarrow \mathbf{R}$.[29−31] It has also been found in aa_3 that the reduction of $\mathbf{O_H}$ is coupled to proton translocation, while the reduction of **O** is not.[29−31] From these variations in kinetics, some significant structural differences between $\mathbf{O_H}$ and **O** are expected, but these specific differences are not at all evident. It has been a hot topic in the past 30 years and is still under debate which species bridges the Fe_{a3}^{3+} and Cu_B^{2+} sites in the resting "as-isolated" **O** state, despite various spectral and structural analyses.[32−40]

The electron density between Fe_{a3} and Cu_B in the as-isolated oxidized aa_3 type C*c*Os from *Paracoccus denitrificans* (*Pd*) and *Rhodobacter sphaeroides* (*Rs*) was originally interpreted as a H_2O and an OH^- ligand.[33,34] Later, on the basis of the high-resolution X-ray crystal structures of the oxidized C*c*O's from *Pd* (PDB code 3HB3, 2.25 Å resolution)[35] and from bovine heart (PDB code 2ZXW, 1.95 Å resolution),[36] two research groups have independently proposed that a peroxide dianion (O_2^{2-}) bridges the Fe_{a3} and Cu_B in the DNC. Similarly, strong electron density for a peroxide type dioxygen species (O1−O2) bridging the Fe_{a3} and Cu_B DNC was also observed in the high-resolution (1.8 Å) X-ray crystal structures (PDB entries 3S8G and 3S8F) of ba_3 C*c*O from *Tt* (see Figure 2).[37] Further, the peroxide type species in the resting oxidized DNC was also observed by the X-ray free-electron laser (XFEL) experiment (1.9 Å resolution).[38] Different groups reported slightly different O1−O2 distances of around 1.5−1.7 Å. Recently, Andersson et al. reported a radiation-damage-free oxidized ba_3 C*c*O structure (2.3 Å resolution) at room temperature, in which a single hydroxide or a water molecule resides between the Fe_{a3} and Cu_B sites.[39] However, the very recent low-dose high-energy X-ray data analysis on the oxidized-resting bovine heart C*c*O again showed the peroxide-type electron density between the Fe_{a3} and Cu_B sites.[40]

Theoretically, Kaila et al. proposed through their quantum chemical calculations that this bridging ligand in the resting oxidized DNC of bovine heart C*c*O is dioxygen (O_2), which may be reduced to superoxide ($O_2^{\bullet-}$) in the X-ray beam.[41] However, their calculated O−O distances of 1.29−1.32 Å for O_2 or $O_2^{\bullet-}$ bridges are much shorter than the apparent O−O distances observed in the X-ray structures. Further, we are not aware of any experimental evidence favoring the presence of molecular oxygen (O_2) between the oxidized Fe^{3+} and Cu^{2+} metal centers. If the affinity of O_2 binding with Fe^{3+} and Cu^{2+} is low, the O−O species with high occupancy observed in the X-ray crystal structures cannot be molecular O_2. We have therefore also performed density functional theory (DFT) calculations[42] on the ba_3 C*c*O from *Tt* on the basis of the 3S8G[37] X-ray crystal structure with O_2^{2-}, $O_2^{\bullet-}$, HO_2^-, or H_2O_2 in the bridging position. These calculations have shown that the geometry optimized DNC structures with either O_2^{2-} or $O_2^{\bullet-}$ as the bridging species would have large structural discrepancies in comparison with the X-ray crystal structure.[42] When H_2O_2 was put in between the Fe_{a3}^{2+} and Cu_B^{+} sites (Fe_{a3}^{3+}

https://dx.doi.org/10.1021/acs.inorgchem.0c00724
Inorg. Chem. 2020, 59, 8906−8915

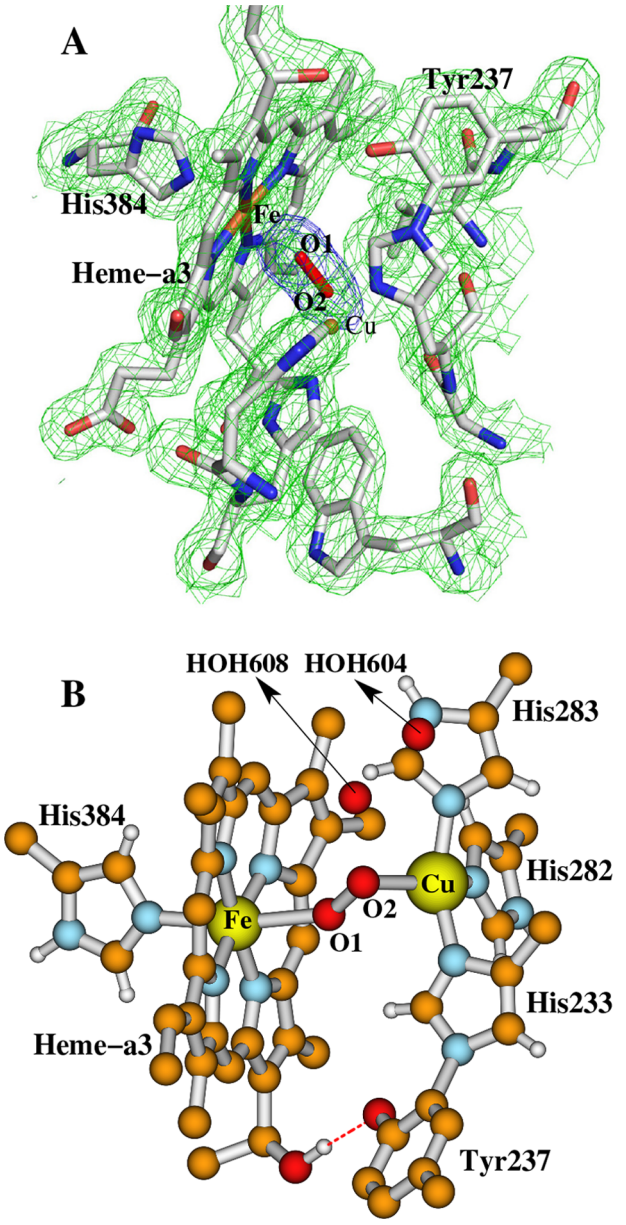

Figure 2. Dinuclear center (DNC) of the X-ray crystal structure 3S8G of ba_3 C*c*O from *Thermus thermophilus* (*Tt*).[37] (A) The electron density map adapted with permission from Figure 5 of ref 37. Copyright © 2011 Tiefenbrunn et al. (B) The ball and stick structure of this DNC in a different orientation.

and Cu_B^{2+} metal sites were assumed to be reduced in the X-ray beam),[37] the O−O bond broke during the geometry optimizations regardless of the spin state of Fe_{a3}^{2+}.[42] Also, it is well-known experimentally that, in the oxidized resting **O** state in ba_3, the dinuclear center is closed and reacts only very slowly with Fe_{a3} ligands, including H_2O_2. (The aa_3 enzyme shows more access to H_2O_2 in state **O**.) The dinuclear site in ba_3 only opens up for binding of H_2O_2 and reaction after a single-electron photoactivated injection into the enzyme.[43,44] The presence then of H_2O_2 or related species within the active site of the oxidized resting **O** state in ba_3 would be unexplained, aside from possible radiation-induced reactions.

Finally, our previous calculations indicated that the O1−O2 species observed in the DNC of the X-ray crystal structure was best represented as HO_2^-, which may be a product of the photoreaction of the H_2O/OH^- ligands with $2e^-$ transfer to the adjacent oxidized Fe_{a3}^{3+} and Cu_B^{2+} sites in the X-ray beam.[42] However, in evaluating the most likely and unlikely physical explanation for the observed electron density map, we need to take into account that the operating physical mechanism will produce atomic structures that represent both a spatial and time average over billions of enzyme molecules. While some effects due to the X-ray irradiation may be observable with careful attention to the time course, these effects are not likely to be dominant when they are averaged over billions of structural sites. Indeed, as we now show in the Results and Discussion, our current calculations demonstrate that the $Fe_{a3}^{3+}-H_2O\cdots OH^-Cu_B^{2+}/Fe_{a3}^{3+}-OH^-\cdots H_2O-Cu_B^{2+}$ type structures are also unlikely to represent the resting state of the DNC, and the observed O1−O2 peroxide type electron density between the two metal centers is most likely the overlap of electron densities of single water molecules positioned somewhere between O1 and O2 in different DNCs with almost the same energy. The effective electron density averaging occurs because of the long-range averaging over molecular subunits in Fourier (reciprocal) space converted back to real coordinate space (Cartesian space).

2. CALCULATION METHODS

The starting geometries of the DNC model clusters studied in this paper were established on the basis of the Cartesian coordinates of the ba_3 C*c*O X-ray crystal structure 3S8G.[37] All calculations were performed using the DFT dispersion-corrected OLYP-D3(BJ)[45] functional implemented within the ADF2017 software package.[46−48] Goerigk et al. assessed 217 variations of dispersion-corrected and -uncorrected density functional approximations and carried out a detailed analysis to identify reliable approaches based on the analysis of the GMTKN55 benchmark database for general main-group thermochemistry, kinetics, and noncovalent interactions.[49] Their studies have shown that OLYP-D3(BJ) is one of the best three GGA functionals overall, outperforming all dispersion-corrected meta-GGAs except for SCAN-D3(BJ).[49]

Our geometry optimization calculations were performed using the broken-symmetry[50−52]/OLYP-D3(BJ)[45]/TZP plus COSMO[15,26,53−56] solvation model methodology. The inner cores of C(1s), N(1s), and O(1s) were treated by the frozen core approximation.

Starting from the active $\mathbf{O_H}[Fe_{a3}^{3+}-OH^-Cu_B^{2+}]$ state model, we will examine whether there are H_2O/OH^- ligands or a H_2O molecule between the Fe_{a3}^{3+} and Cu_B^{2+} sites in the resting as-isolated **O** state through energetic and pK_a calculations. The whole structure of our DNC model for the $\mathbf{O_H}$ state is shown in Figure 3. For a clearer view, the top portion of this cluster is shown in Figure 4I, and the central $Fe_{a3}^{3+}-OH^-Cu_B^{2+}$ part of the model is given in Figure 4II. In our $\mathbf{O_H}$ model, the bridging OH^- is H-bonding with a water molecule, which originates from the H_2O ligand of Cu_B in the prior state **F**.

When each model is constructed from the X-ray crystal structure 3S8G,[37] the C_α atoms of Tyr237, His233, His282, His283, Asp372, His376, and His384 are each replaced with a link H atom along the original $C_\beta-C_\alpha$ direction with a $C_\beta-H_{link}$ distance of 1.09 Å. The C_β of Arg449 and C_{228} of the geranyl side chain of the a_3-heme are also replaced with a H_{link} atom. During the geometry optimizations, except for the H_{link} atom on the geranyl side chain of the a_3-heme, the positions of all other H_{link} atoms are fixed. Note that, in order to avoid the energy difference caused by the different H-bonding patterns, the two water molecules HOH604 and HOH608 above the O1−O2 species found in the 3S8G X-ray crystal structure are not included in our current models. We have geometry-optimized our DNC model clusters with the Fe_{a3}^{3+} site in different spin states (low spin, intermediate spin, and high spin). Our calculations show that the intermediate-spin-Fe_{a3}^{3+} state is generally lower in energy than the corresponding high-spin-Fe_{a3}^{3+} state for each model cluster studied

https://dx.doi.org/10.1021/acs.inorgchem.0c00724
Inorg. Chem. 2020, 59, 8906−8915

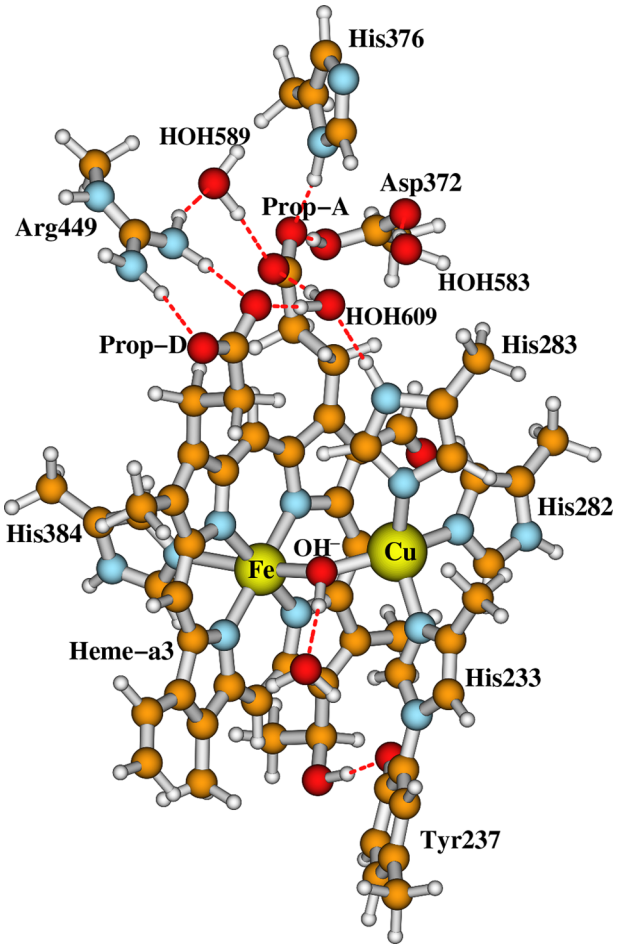

Figure 3. Our whole DNC model for state $\mathbf{O_H}$. Clearer views for both the top cluster and the central Fe_{a3}^{3+}–OH^-–Cu_B^{2+} portion of the model are given in Figure 4I,II, respectively.

here. However, the rR and EPR experimental data suggest that the Fe_{a3}^{3+} is high spin in both the active $\mathbf{O_H}$ and the resting **O** states.[5,57] One needs more experimental data and higher-level theoretical calculations to determine whether different spin states of Fe_{a3}^{3+} can coexist in the $\mathbf{O_H}$ and the resting **O** states. In fact, the existence of intermediate-/low-spin-Fe_{a3} states in the resting **O** DNCs may be temperature-dependent, since Mössbauer spectroscopy experiments on *Tt* ba_3[58] and c_1aa_3[59] have shown the coexistence of different high-spin and "low-spin" (which might also be intermediate-spin according to the isomer shift and quadrupole splitting values) Fe_{a3}^{3+} species at very low temperature (4.2 K), and the "low-spin" Fe_{a3}^{3+} species changes to high spin as the temperature is increased above 190 K.[58] These spin states may exhibit spin crossover, which depends on a sensitive balance between the respective energies and entropies. For simplicity, we will present our calculated results in which the high-spin (HS) Fe_{a3}^{3+} site is antiferromagnetically (AF) coupled with the Cu_B^{2+} site and put the results of the intermediate- and low-spin-Fe_{a3}^{3+} states in the Supporting Information. Note that all conclusions we find for the HS-Fe_{a3}^{3+} states in the following section will remain the same if the Fe_{a3}^{3+} is in the intermediate-spin state.

3. RESULTS AND DISCUSSION

Our calculated energies and the main geometric and Mulliken net spin population properties of the geometry-optimized $\mathbf{O_H}[Fe_{a3}^{HS,3+}–OH–Cu_B^{2+}]$ state and the possible $\mathbf{O}[Fe_{a3}^{HS,3+}–H_2O\cdots OH^-–Cu_B^{2+}]$ and $\mathbf{O}[Fe_{a3}^{HS,3+}–OH^-\cdots H_2O–Cu_B^{2+}]$ states are given in the first three rows of Table 1. The central portions of the $Fe_{a3}^{HS,3+}–H_2O\cdots OH^-–Cu_B^{2+}$ and $Fe_{a3}^{HS,3+}–OH^-\cdots H_2O–Cu_B^{2+}$ DNC clusters are given in Figure 4III,IV, respectively. The net spin populations from Mulliken population analysis are the main indication of the spin state for the Fe_{a3}^{3+} site. In the ideal ionic limit, the net unpaired spin populations for HS-Fe_{a3}^{3+} and Cu_B^{2+} are 5 and 1, respectively. However, because of the metal–ligand covalency, the calculated net spin magnitudes for the Fe_{a3}^{3+} and Cu_B^{2+} sites are smaller than their corresponding ionic limits. The opposite signs for the spin densities of Fe_{a3}^{3+} and Cu_B^{2+} sites indicate the AF coupling. Our calculated net spins on Fe_{a3}^{3+} and Cu_B^{2+} show that we obtained the HS-Fe_{a3}^{3+} AF-coupled to the Cu_B^{2+} state for each cluster.

$\mathbf{O_H}$ is a metastable catalytically active state, which decays to the relaxed **O** state when no electron transfers to the DNC. Therefore, state **O** is lower in energy than $\mathbf{O_H}$. However, our calculations show that both the $Fe_{a3}^{HS,3+}–H_2O\cdots OH^-–Cu_B^{2+}$ and $Fe_{a3}^{HS,3+}–OH^-\cdots H_2O–Cu_B^{2+}$ states are higher in energy (by >6 kcal mol^{-1}) than the $Fe_{a3}^{HS,3+}–OH–Cu_B^{2+}$ state. Further, the O···O distances (~2.5 Å) in $Fe_{a3}^{HS,3+}–H_2O\cdots OH^-–Cu_B^{2+}$ and $Fe_{a3}^{HS,3+}–OH^-\cdots H_2O–Cu_B^{2+}$ structures are ~1 Å longer than the apparent O1–O2 distance found from the 3S8G X-ray crystal structure (see the last row of Table 1). Therefore, the DNC of the resting as-isolated **O** state is not likely in the $Fe_{a3}^{HS,3+}–H_2O\cdots OH^-–Cu_B^{2+}$ or the $Fe_{a3}^{HS,3+}–OH^-\cdots H_2O–Cu_B^{2+}$ form.

Next, we examine whether a water molecule is preferred residing between the Fe_{a3}^{3+} and Cu_B^{2+} sites in the as-isolated **O** state. We then protonated the bridging OH^- in the state $\mathbf{O_H}[Fe_{a3}^{3+}–OH^-–Cu_B^{2+}]$, kept the H-bonding H_2O molecule, and optimized the structure. We find that, by modification of the position of the proton added to the bridging OH^- or the orientation of the H-bonding H_2O molecule, the geometry optimizations will end in different minima with different Fe–O, Cu–O, and Fe···Cu distances, but with very similar energies. The central $Fe_{a3}^{HS,3+}–H_2O–Cu_B^{2+}$ structures of four major optimized geometries (a–d) are shown in Figure 4V–VIII, and their main bond distances and energies are given in rows 4–7 of Table 1.

In the optimized structure $Fe_{a3}^{HS,3+}–H_2O–Cu_B^{2+}$(a) (Figure 4.V), the H_2O molecule binds with the Fe_{a3}^{3+} site with Fe-O distance of 2.39 Å. In $Fe_{a3}^{HS,3+}–H_2O–Cu_B^{2+}$(b) (Figure 4VI), the H_2O molecule is in between Fe_{a3}^{3+} and Cu_B^{2+} and does not bind with either site (with Fe–O and Cu–O distances of 2.47 and 2.77 Å, respectively). Although structurally different, both structures are essentially at the same energy. In structures $Fe_{a3}^{HS,3+}–H_2O–Cu_B^{2+}$(c) (Figure 4VII) and $Fe_{a3}^{HS,3+}–H_2O–Cu_B^{2+}$(d) (Figure 4VIII), the H_2O molecule binds with the Cu_B site (with Cu–O distances of 2.21 and 2.20 Å, respectively) in different orientations. In $Fe_{a3}^{HS,3+}–H_2O–Cu_B^{2+}$(c), the H_2O molecule tilts up and has an H-bonding interaction with one of the N atoms of the heme ring; in $Fe_{a3}^{HS,3+}–H_2O–Cu_B^{2+}$(d), however, the H_2O simply moves closer to Cu_B^{2+} starting from the bridging position. $Fe_{a3}^{HS,3+}–H_2O–Cu_B^{2+}$(c) and $Fe_{a3}^{HS,3+}–H_2O–Cu_B^{2+}$(d) also have nearly the same energy. In fact, all four $Fe_{a3}^{HS,3+}–H_2O–Cu_B^{2+}$(a–d) structures are close in energy, with a maximum difference of 0.7 kcal mol^{-1}. Since these four structures have one more proton than the $\mathbf{O_H}[Fe_{a3}^{HS,3+}–OH^-–Cu_B^{2+}]$ state, in order to compare the energetic stabilities, we calculated the pK_a of the H_2O molecules in the four $Fe_{a3}^{HS,3+}–H_2O–Cu_B^{2+}$(a–d) structures using the equation[26,42,60,61]

https://dx.doi.org/10.1021/acs.inorgchem.0c00724
Inorg. Chem. 2020, 59, 8906–8915

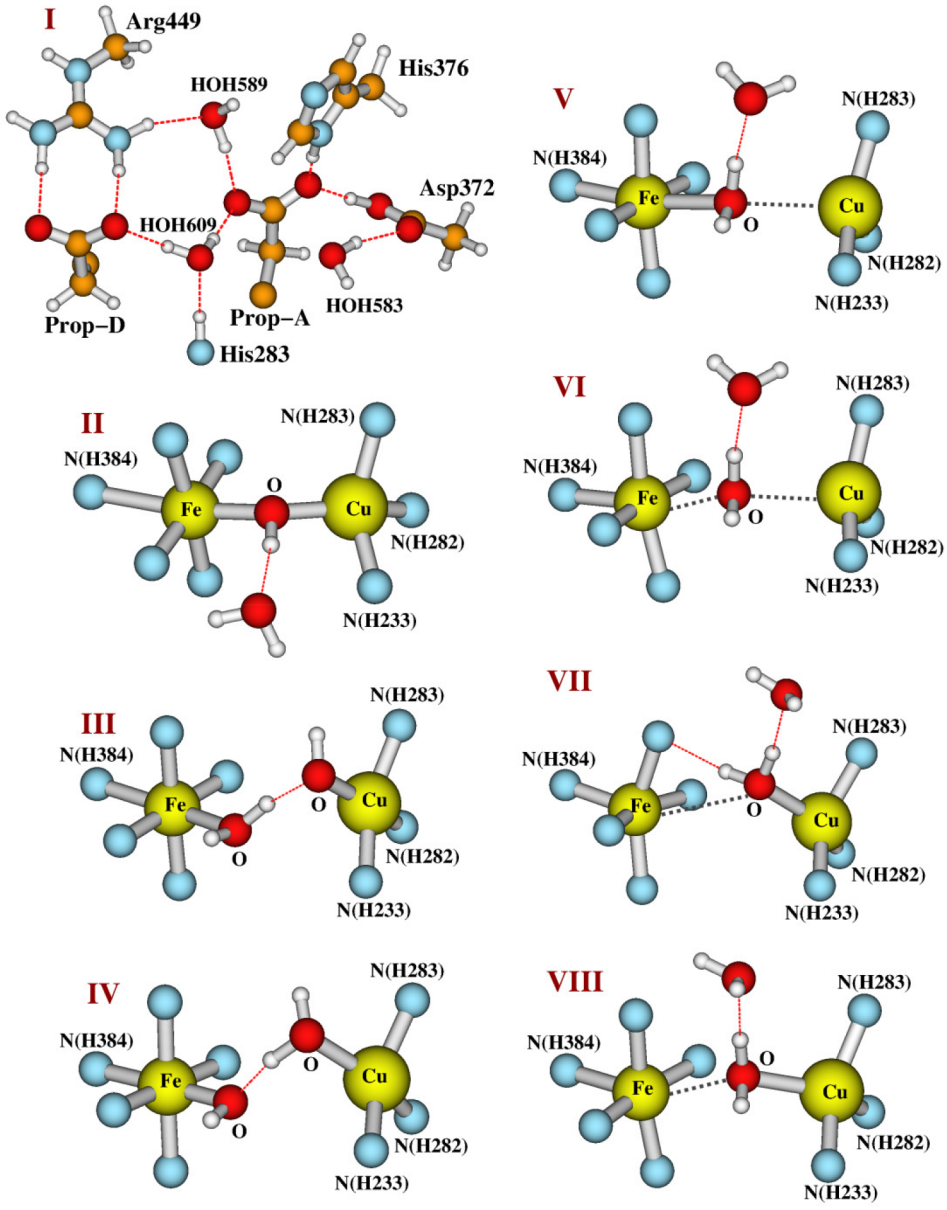

Figure 4. A closer look at the top (I) and the central (II–VIII) portions of the DNC model clusters studied here (see Table 1). The rest of each model is similar to what was shown in Figure 3. Legend: (II) $\mathbf{O_H}[Fe^{3+}_{a3}–OH^––Cu^{2+}_B]$ state; (III) $Fe^{3+}_{a3}–H_2O\cdots OH^––Cu^{2+}_B$ model state; (IV) $Fe^{3+}_{a3}–OH^–\cdots H_2O–Cu^{2+}_B$ model state; (V) $Fe^{3+}_{a3}–H_2O–Cu^{2+}_B$(a); (VI) $Fe^{3+}_{a3}–H_2O–Cu^{2+}_B$(b); (VII) $Fe^{3+}_{a3}–H_2O–Cu^{2+}_B$(c); (VIII) $Fe^{3+}_{a3}–H_2O–Cu^{2+}_B$(d). Note that structures V–VIII are four major optimized structures (see the Results and Discussion and Table 1) with very similar energies obtained by protonating the bridging $OH^–$ ligand in $\mathbf{O_H}[Fe^{3+}_{a3}–OH^––Cu^{2+}_B]$ (model II).

$$1.37\mathrm{p}K_a = E(A^-) - E(AH) + E(H^+) + \Delta G_{sol}(H^+, 1\ \mathrm{atm}) - T\Delta S_{gas}(H^+) + \Delta ZPE + (5/2)RT \quad (1)$$

where $E(A^-)$ and $E(AH)$ are the calculated total energies of the deprotonated (A^-, here $\mathbf{O_H}[Fe^{HS,3+}_{a3}–OH^––Cu^{2+}_B]$) and protonated (AH, here the four $Fe^{HS,3+}_{a3}–H_2O–Cu^{2+}_B$(a–d)) states. In ADF, the "total energy" of the system is defined relative to a sum of atomic fragments (spherical spin-restricted atoms). The calculated gas-phase energy of a proton $E(H^+)$ is therefore relative to a spin-restricted hydrogen atom. $\Delta G_{sol}(H^+,1\ \mathrm{atm})$ is the solvation free energy of a proton at 1 atm pressure. We use the "best available" experimental value of -264.0 kcal mol^{-1} for this term, on the basis of an analysis of cluster-ion solvation data.[62−65] For $E(H^+)$, here we take the empirically corrected values 293.1 kcal mol^{-1} (i.e., 12.71 eV) for OLYP based on experimental standard hydrogen electrode energy and the proton solvation free energy (see Appendix in ref 60). The translational entropy contribution to the gas-phase free energy of a proton is taken as $-T\Delta S_{gas}(H^+) = -7.8$ kcal mol^{-1} at 298 K and 1 atm pressure.[66] $(5/2)RT$ = 1.5 kcal mol^{-1} includes the proton translational energy $(3/2)RT$ and $PV = RT$.[66] The term ΔZPE is the zero-point energy difference for the deprotonated state (A^-) minus the protonated state (AH), and it was estimated as $\Delta ZPE = -7.7$ kcal mol^{-1} for $OH^–/H_2O$ by only optimizing the geometries (and then performing frequency calculations) of an $OH^–$ and an H_2O molecule within the COSMO solvation model.

The calculated pK_as of the H_2O molecule in each of the $Fe^{HS,3+}_{a3}–H_2O–Cu^{2+}_B$(a–d) states are also given in Table 1. They are between 11.7 and 12.2, indicating that the $Fe^{HS,3+}_{a3}$–

https://dx.doi.org/10.1021/acs.inorgchem.0c00724
Inorg. Chem. 2020, 59, 8906−8915

Table 1. OLYP-D3(BJ) Calculated Geometrical, Energetic, and Net Spin Properties of the Optimized DNC Clusters in $Fe_{a3}^{HS,3+}$−OH^-−Cu_B^{2+}, $Fe_{a3}^{HS,3+}$−H_2O···OH^-−Cu_B^{2+}, $Fe_{a3}^{HS,3+}$−OH^-···H_2O−Cu_B^{2+}, and $Fe_{a3}^{HS,3+}$−H_2O−Cu_B^{2+} States[a]

	geometry (Å)								net spin[f]			
structure[b]	Fe−N(H384)	Fe−O	Cu−O	O···O	Fe···Cu	E^c	Q^d	$pK_a(H_2O)^e$	Fe_{a3}	O(Fe)/O(Cu)	Cu_B	Y237
$Fe_{a3}^{HS,3+}$−OH^-−Cu_B^{2+}	2.50	1.99	2.04		3.73	0.0	0		4.08	0.12	−0.39	−0.25
$Fe_{a3}^{HS,3+}$−H_2O···OH^-−Cu_B^{2+}	2.18	2.17	1.95	2.50	4.78	6.3	0		4.08	0.08/−0.16	−0.50	0.11
$Fe_{a3}^{HS,3+}$−OH^-···H_2O−Cu_B^{2+}	2.28	1.98	2.13	2.45	4.64	6.6	0		4.12	0.20/−0.03	−0.39	−0.36
$Fe_{a3}^{HS,3+}$−H_2O−Cu_B^{2+}(a)	2.11	2.39	2.94		4.98	−1.5	1	12.1	4.11	0.04	−0.24	−0.62
$Fe_{a3}^{HS,3+}$−H_2O−Cu_B^{2+}(b)	2.12	2.47	2.77		4.90	−1.6	1	12.2	4.10	0.04	−0.25	−0.61
$Fe_{a3}^{HS,3+}$−H_2O−Cu_B^{2+}(c)	2.06	3.55	2.21		4.73	−1.2	1	11.9	4.06	−0.01	−0.36	−0.36
$Fe_{a3}^{HS,3+}$−H_2O−Cu_B^{2+}(d)	2.09	3.26	2.20		4.73	−0.9	1	11.7	4.09	−0.02	−0.35	−0.44
3S8G[g]	2.22	2.39	2.25	1.52	4.92							

[a]See Figure 4. [b]Geometries were optimized in the broken-symmetry state with high-spin (HS) Fe_{a3}^{3+} AF-coupled to the Cu_B^{2+} site. [c]Calculated broken-symmetry state energies (offset by −26336.6 kcal mol^{-1}). [d]The net charge of the model clusters. [e]The $pK_a(H_2O)$ values were calculated for the process $Fe_{a3}^{HS,3+}$−OH^-−Cu_B^{2+} → $Fe_{a3}^{HS,3+}$−H_2O−Cu_B^{2+}(a−d). [f]The Mulliken net spin populations on Fe_{a3}^{3+}, O of the bridging OH^-/H_2O, Cu_B^{2+}, and the heavy atoms of the Tyr237−O^- side chain (the sum total). [g]The X-ray crystal structure.[37]

H_2O−Cu_B^{2+}(a−d) states are energetically much more stable than the $\mathbf{O_H}[Fe_{a3}^{HS,3+}$−$OH^-$−$Cu_B^{2+}]$ state. We therefore speculate that it is a water molecule between the Fe_{a3}^{3+} and Cu_B^{2+} sites in the resting as-isolated **O** state. However, an extended electron density, which was interpreted as a dioxygen molecule, was observed between Fe_{a3}^{3+} and Cu_B^{2+} in the DNC of the X-ray crystal structures.[35−37] Since our initial geometries of our DNC model structures are constructed on the basis of the Cartesian coordinates of the X-ray crystal structure 3S8G,[37] to compare our optimized structures $Fe_{a3}^{HS,3+}$−H_2O−Cu_B^{2+}(a−d) with 3S8G, we superimpose the Cartesian coordinates of the central portions of the five structures together. The overlapped structures are shown in Figure 5 with two orientations: A and B. The colors of the atoms in the different structures are as follows: 3S8G, silver; $Fe_{a3}^{HS,3+}$−H_2O−Cu_B^{2+}(a), orange; $Fe_{a3}^{HS,3+}$−H_2O−Cu_B^{2+}(b), purple; $Fe_{a3}^{HS,3+}$−H_2O−Cu_B^{2+}(c), blue; $Fe_{a3}^{HS,3+}$−H_2O−Cu_B^{2+}(d), green.

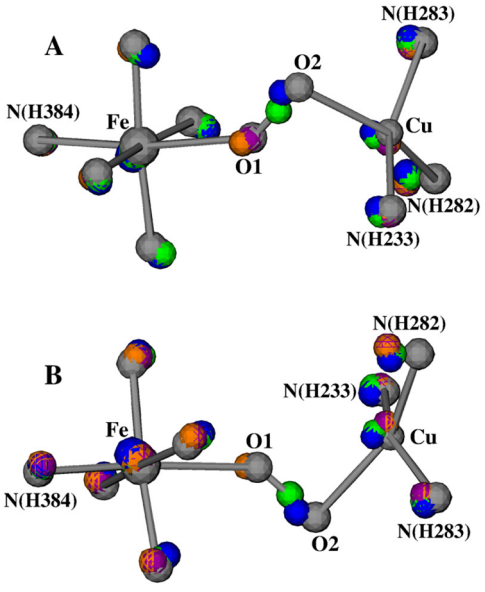

Figure 5. Overlap of the central portions of the following DNC structures (see Table 1): silver, 3S8G X-ray crystal structure; orange, $Fe_{a3}^{HS,3+}$−H_2O−Cu_B^{2+}(a); purple, $Fe_{a3}^{HS,3+}$−H_2O−Cu_B^{2+}(b); blue, $Fe_{a3}^{HS,3+}$−H_2O−Cu_B^{2+}(c); and green, $Fe_{a3}^{HS,3+}$−H_2O−Cu_B^{2+}(d). (A) and (B) are the views of this overlap from two different angles. For clarity, the H-bonding water molecules and the hydrogen atoms are not shown.

During our geometry optimizations, the Cu_B site and its ligands move slightly more than the heme-Fe_{a3} site. Now focusing on the positions of the central oxygen atoms, we do see that the four O atoms in the optimized structures align with the 3S8G O1−O2 directions very well. The orange and purple O atoms are close to the O1 position in 3S8G, the blue O atom is near O2, and the green O atom is in about the middle between O1 and O2. This supports our proposal that the electron density around O1−O2 in the X-ray crystal structures represents the overlap of the electron density of one water molecule that is in different positions along O1−O2 in different C*c*O molecules in a crystal.

For clarity, the water molecule that has an H-bonding interaction with the ligand H_2O in each of the four geometry-optimized structures is not shown in Figure 5. In 3S8G, a water molecule (HOH608) was seen 3.01 Å above the position of O2. Therefore, HOH608 may have an H-bonding interaction with the H_2O ligand in a position as in Fe_{a3}^{3+}−H_2O−Cu_B^{2+}(c) (Figure 4VII). No other H_2O molecules were identified within the H-bonding distances around O1−O2 in 3S8G. This means that not all C*c*O molecules in the crystal have an H_2O molecule H-bonding to the H_2O ligand, and even if there is an H-bonding H_2O molecule in some of the C*c*O DNCs, the H-bonding patterns and the positions of the H-bonding H_2O molecules may differ; therefore, they may not be identified in the X-ray crystal structure.

Since it is not clear whether there is an H-bonding H_2O molecule in the DNC of the **O** state, we removed the H-bonding H_2O from the $Fe_{a3}^{HS,3+}$−H_2O−Cu_B^{2+}(a−d) structures and optimized the geometries again. The central portions of the corresponding optimized structures (S) are given as S1−S4 in Figure 6, respectively. Their main bond distances and the calculated energies are given in Table 2.

Without the H-bonding H_2O molecule, the binding of the H_2O ligand with the two metal sites, especially with the Fe_{a3}^{3+} site, are weakened. For instance, from $Fe_{a3}^{HS,3+}$−H_2O−Cu_B^{2+}(a) to S1, the H_2O dissociates from the Fe_{a3}^{3+} site (from an Fe−O distance of 2.39 Å) and moves to about the middle between Fe_{a3}^{3+} and Cu_B^{2+} (Fe−O, 2.61 Å; Cu−O, 2.82 Å). S1 has the longest calculated Fe_{a3}^{3+} and Cu_B^{2+} distance of 5.03 Å. S3 differs from the $Fe_{a3}^{HS,3+}$−H_2O−Cu_B^{2+}(c) structure with slightly elongated Cu−O and Fe−Cu distances. S2 and S4 look very similar and have almost the same energy, but with different

https://dx.doi.org/10.1021/acs.inorgchem.0c00724
Inorg. Chem. 2020, 59, 8906−8915

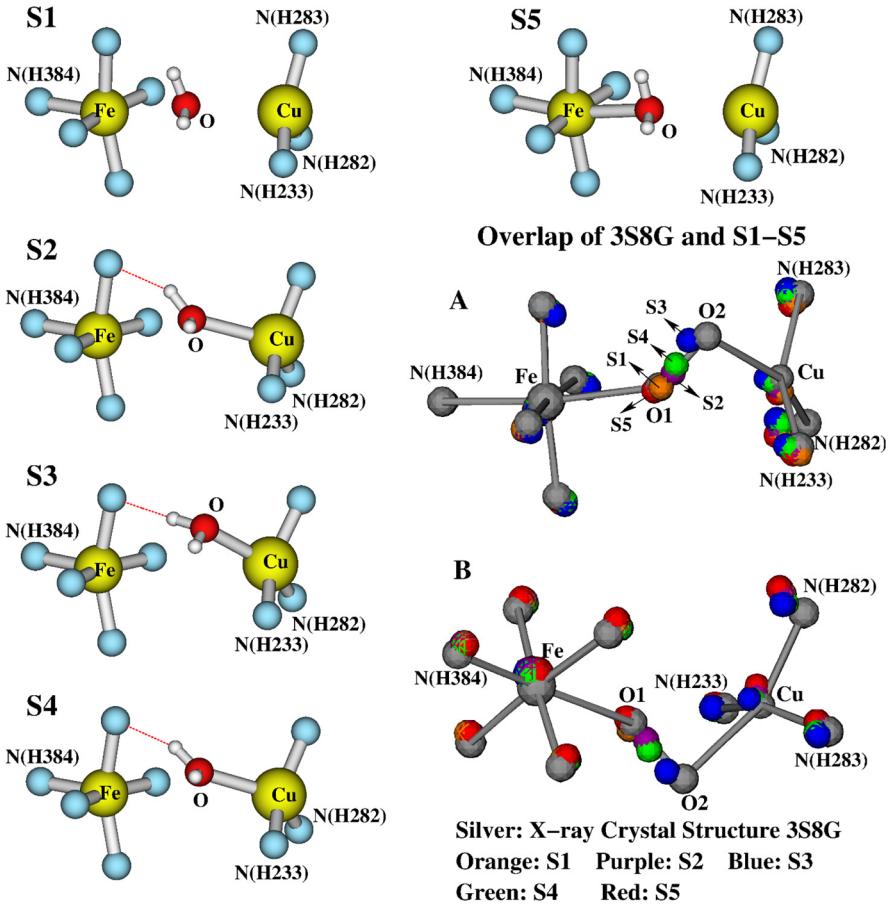

Figure 6. Structures (S) S1–S4 (see Table 2): the central portions of the optimized geometries after removing the H-bonding H_2O molecule from the $Fe_{a3}^{HS,3+}$–H_2O–Cu_B^{2+}(a–d) structures (see Figure 4V–VIII). S5 is a constrained geometry optimized structure with a fixed Fe–O distance at 2.39 Å. (A) and (B) show the overlap of S1–S5 with the X-ray crystal structure 3S8G in two different viewing angles (see also Figure 7).

Table 2. Geometry Optimized $Fe_{a3}^{HS,3+}$–H_2O–Cu_B^{2+} DNC Structures and Energies, in Which No Water Molecule H-Bonding to the H_2O Ligand[a]

	distance (Å)			
structure[b]	Fe–O	Cu–O	Fe···Cu	E^c (kcal/mol)
S1	2.61	2.82	5.03	1.4
S2	2.97	2.52	4.98	0.3
S3	3.54	2.29	4.76	0.0
S4	3.07	2.41	4.87	0.6
S5[d]	2.39	2.81	4.91	0.8

[a]See Figures 6 and 7. [b]Geometries (S1–S5) were optimized in the broken-symmetry state with high-spin Fe_{a3}^{3+} AF-coupled to the Cu_B^{2+} site. [c]Calculated broken-symmetry state energies (offset by −26004.7 kcal mol^{-1}). Note that Fe_{a3}^{3+} and Cu_B^{2+} are very weakly coupled. The F-coupled calculations on these structures yield essentially the same energy as the corresponding broken-symmetry state. [d]The Fe–O distance was fixed at 2.39 Å during this geometry optimization.

Fe–O, Cu–O, and Fe–Cu distances. The calculated energies among S2–S4 are within 1 kcal mol^{-1}. Although S1 has the highest calculated energy, it is only 1.4 kcal mol^{-1} higher than S3. Further, to see how high the energy would be if the H_2O molecule is close to the Fe_{a3}^{3+} site as in the structure $Fe_{a3}^{HS,3+}$–H_2O–Cu_B^{2+}(a), we reoptimized the geometry of S1 with a fixed Fe–O distance at 2.39 Å. The constraint optimized structure is also shown in Figure 6 as S5, and its geometric and energetic properties are also given in Table 2. It turned out that the calculated energy of S5 is very close to those of S2 and S4 and is only 0.8 kcal mol^{-1} higher than that of S3. Because of the very similar energies, in principle, the structures S1–S5 may coexist in the DNCs of different CcO molecules.

Similar to the case for Figure 5, in Figure 6A,B, we have also shown the overlap of the DNCs of S1–S5 and the X-ray crystal structure 3S8G in two different viewing angles. The colors of the atoms in different structures are as follows: 3S8G, silver; S1, orange; S2, purple; S3, blue; S4, green; S5, red. In the overlap structure, the H_2O molecules in S1 and S5 are in the vicinity of the O1 position in 3S8G, the H_2O in S3 is close to the position of O2, and the H_2O molecules in S2 and S4 are located between O1 and O2. The same overlap structure is also shown in Figure 7, where the electron density map is reconstructed from the 3S8G data file. Again, this supports the proposal that in the resting **O** state the H_2O molecule may reside at different positions along the O1–O2 direction between the Fe_{a3}^{3+} and Cu_B^{2+} sites in different enzyme molecules.

Further, although the structures and energies for $Fe_{a3}^{HS,3+}$–H_2O–Cu_B^{2+}(a–d) and S1–S5 given in Tables 1 and 2 are obtained from broken-symmetry state calculations in which the HS-Fe_{a3}^{3+} is AF-coupled to Cu_B^{2+}, the coupling between the HS-Fe_{a3}^{3+} and Cu_B^{2+} sites appears to be very weak. Our $Fe_{a3}^{HS,3+}$-Cu_B^{2+} ferromagnetically coupled (F-coupled) calculations show that each of these structures also represents an optimization-converged geometry in the F-coupled state with essentially the same energy as the corresponding broken-symmetry state.

https://dx.doi.org/10.1021/acs.inorgchem.0c00724
Inorg. Chem. 2020, 59, 8906–8915

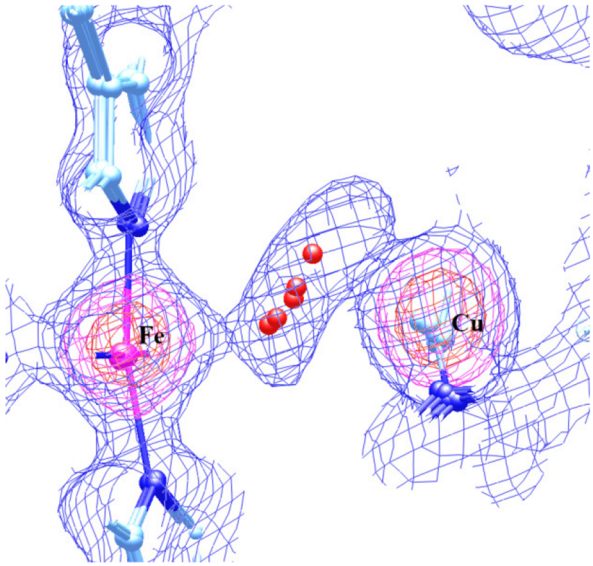

Figure 7. Overlap of the structures S1−S5 (also see Table 2 and Figure 6) with the electron density map that was reconstructed from the X-ray crystal structure 3S8G data file.

Therefore, both $Fe_{a3}^{HS,3+}$-Cu_B^{2+} AF-coupled and F-coupled configurations of the DNCs may coexist in the resting **O** state.

4. CONCLUSIONS

Starting from the $\mathbf{O_H}[Fe_{a3}^{3+}-OH^--Cu_B^{2+}]$ DNC structure of the active oxidized state C*c*O, where a hydroxo bridges the Fe_{a3}^{3+} and the Cu_B^{2+} sites, we have studied the feasible DNC structures of the resting as-isolated oxidized **O** state. Our calculations show that the **O** state is not likely in the $Fe_{a3}^{3+}-H_2O\cdots OH^-Cu_B^{2+}$ or the $Fe_{a3}^{3+}-OH^-\cdots H_2O-Cu_B^{2+}$ forms, where an H_2O/OH^- binds with Fe_{a3}^{3+}/Cu_B^{2+} and the H_2O and OH^- ligands H-bond with each other, since both the $Fe_{a3}^{3+}-H_2O\cdots OH^-Cu_B^{2+}$ and the $Fe_{a3}^{3+}-OH^-\cdots H_2O-Cu_B^{2+}$ structures are higher in energy than the $\mathbf{O_H}[Fe_{a3}^{3+}-OH^-Cu_B^{2+}]$ state. Also, the structures of these metal bridging $OH^-\cdots H_2O$ systems show O···O distances in poor agreement with the X-ray structures of ba_3 and aa_3 C*c*Os. Further, our pK_a calculations show that the bridging OH^- ligand in the $\mathbf{O_H}[Fe_{a3}^{3+}-OH^-Cu_B^{2+}]$ state energetically prefers to be protonated at neutral pH. We therefore propose that a water molecule is between the Fe_{a3}^{3+} and Cu_B^{2+} sites in the resting **O** state of C*c*O. Our calculations further suggest that the H_2O molecule can bind with either the Fe_{a3}^{3+} or the Cu_B^{2+} site or it can stay at various positions between the Fe_{a3}^{3+} and Cu_B^{2+} sites with very similar energies, depending on the $Fe_{a3}^{3+}-Cu_B^{2+}$ distance and whether or not this H_2O molecule has an H-bonding interaction with another H_2O molecule.

The X-ray crystal structures of the oxidized C*c*Os from *Pd* (3HB3),[35] from bovine heart (2ZXW),[36] and from *Tt* (3S8G and 3S8F)[37] all show that there is strong electron density for a dioxygen type species (O1−O2) bridging the Fe_{a3}^{3+} and Cu_B^{2+} in the **O** state. In a crystal structure with ∼1.9 Å resolution, it is actually not possible to tell if the ∼1.5 Å apart O−O species is due to overlapping water molecules or a peroxide, as both models would produce very similar overlapping densities in comparison to the experimental electron density map. Since our initial DNC model structures were constructed on the basis of the Cartesian coordinates of the X-ray crystal structure 3S8G, we then superimposed the 3S8G DNC with several of our geometry-optimized $\mathbf{O}[Fe_{a3}^{3+}-H_2O-Cu_B^{2+}]$ structures that have different H_2O positions between Fe_{a3}^{3+} and Cu_B^{2+} and have very similar calculated energies. The overlap structures show that the H_2O molecules lie between and along the O1−O2 direction in 3S8G. There are billions of C*c*O molecules in the crystal, and the water molecule may occupy one equilibrium position at a given time in a given DNC but different ones at other times or in other DNCs. The positions of the different water molecules may be "locked" after the crystal is rapidly frozen (normally at 100 K). However, even at 100 K, the atoms and the water molecules vibrate around their equilibrium positions. The atomic positions obtained from X-ray diffraction analysis are the averages of billions of unit cells over both time and space. Both dynamic and static disorder comparing DNCs in different C*c*O molecules will contribute to the X-ray structure. We therefore propose that the extended electron density between Fe_{a3}^{3+} and Cu_B^{2+} observed in the X-ray crystal structures is the overlap of the electron density of a water molecule located at different positions in different C*c*O molecules in the crystals.

The change in protonation state and structure from state $\mathbf{O_H}$ to **O** leads to large differences in the electron and proton transfer kinetics for the two different subsequent reaction pathways, $\mathbf{O_H} \rightarrow \mathbf{E_H} \rightarrow \mathbf{R}$ in comparison to $\mathbf{O_H} \rightarrow \mathbf{O} \rightarrow \mathbf{E} \rightarrow \mathbf{R}$, with the sequence of $1e^-$ and $1H^+$ transfers to the reactive oxidized $Fe_{a3}^{3+}-OH^-Cu_B^{2+}$ complex switched. The new structural analysis of state **O** in comparison to $\mathbf{O_H}$ provides a foundation for further exploration of these differences in kinetics.

■ ASSOCIATED CONTENT

Supporting Information

The Supporting Information is available free of charge at https://pubs.acs.org/doi/10.1021/acs.inorgchem.0c00724.

> Calculated low-spin-/intermediate-spin-Fe_{a3}^{3+} results, an analysis which corresponds to the high-spin-Fe_{a3}^{3+} results in Table 1, and the Cartesian coordinates of the structures given in Tables 1 and 2 (PDF)

■ AUTHOR INFORMATION

Corresponding Author

Louis Noodleman − *Department of Integrative Structural and Computational Biology, The Scripps Research Institute, La Jolla, California 92037, United States;* orcid.org/0000-0001-8176-4448; Phone: (858) 784-2840; Email: lou@scripps.edu

Authors

Wen-Ge Han Du − *Department of Integrative Structural and Computational Biology, The Scripps Research Institute, La Jolla, California 92037, United States;* orcid.org/0000-0001-5876-1943

Duncan McRee − *Department of Integrative Structural and Computational Biology, The Scripps Research Institute, La Jolla, California 92037, United States*

Andreas W. Götz − *San Diego Supercomputer Center, , University of California San Diego, La Jolla, California 92093, United States;* orcid.org/0000-0002-8048-6906

Complete contact information is available at: https://pubs.acs.org/10.1021/acs.inorgchem.0c00724

https://dx.doi.org/10.1021/acs.inorgchem.0c00724
Inorg. Chem. 2020, 59, 8906−8915

Notes

The authors declare no competing financial interest.

■ ACKNOWLEDGMENTS

We thank Tzanko Doukov and Aina Cohen for very helpful discussions. We thank the NIH for financial support (R01 GM100934) and thank The Scripps Research Institute for computational resources. This work also used the Extreme Science and Engineering Discovery Environment (XSEDE), which is supported by the National Science Foundation (grant number ACI-1053575, resources at the San Diego Supercomputer Center through award TG-CHE130010 to A.W.G.).

■ REFERENCES

(1) Wikström, M. Active Site Intermediates in the Reduction of O_2 by Cytochrome Oxidase, and Their Derivatives. *Biochim. Biophys. Acta, Bioenerg.* **2012**, *1817*, 468−475.
(2) Kaila, V. R. I.; Verkhovsky, M. I.; Wikström, M. Proton-Coupled Electron Transfer in Cytochrome Oxidase. *Chem. Rev.* **2010**, *110*, 7062−7081.
(3) Konstantinov, A. A. Cytochrome *c* Oxidase: Intermediates of the Catalytic Cycle and Their Energy-Coupled Interconversion. *FEBS Lett.* **2012**, *586*, 630−639.
(4) von Ballmoos, C.; Adelroth, P.; Gennis, R. B.; Brzezinski, P. Proton Transfer in ba_3 Cytochrome *c* Oxidase from *Thermus thermophilus*. *Biochim. Biophys. Acta, Bioenerg.* **2012**, *1817*, 650−657.
(5) Wikström, M.; Krab, K.; Sharma, V. Oxygen Activation and Energy Conservation by Cytochrome *c* Oxidase. *Chem. Rev.* **2018**, *118*, 2469−2490.
(6) Farver, O.; Chen, Y.; Fee, J. A.; Pecht, I. Electron Transfer among the Cu_A, Heme-b and a_3 Centers of *Thermus thermophilus* Cytochrome ba_3. *FEBS Lett.* **2006**, *580*, 3417−3421.
(7) Fee, J. A.; Case, D. A.; Noodleman, L. Toward a Chemical Mechanism of Proton Pumping by the B-Type Cytochrome *c* Oxidases: Application of Density Functional Theory to Cytochrome ba_3 of *Thermus thermophilus*. *J. Am. Chem. Soc.* **2008**, *130*, 15002−15021.
(8) Siletsky, S. A.; Belevich, I.; Jasaitis, A.; Konstantinov, A. A.; Wikström, M.; Soulimane, T.; Verkhovsky, M. I. Time-Resolved Single-Turnover of ba_3 Oxidase from *Thermus thermophilus*. *Biochim. Biophys. Acta, Bioenerg.* **2007**, *1767*, 1383−1392.
(9) Verkhovsky, M. I.; Jasaitis, A.; Verkhovskaya, M. L.; Morgan, J. E.; Wikstrom, M. Proton Translocation by Cytochrome *c* Oxidase. *Nature* **1999**, *400*, 480−483.
(10) Han, S.; Ching, Y. C.; Rousseau, D. L. Primary Intermediate in the Reaction of Oxygen with Fully Reduced Cytochrome *c* Oxidase. *Proc. Natl. Acad. Sci. U. S. A.* **1990**, *87*, 2491−2495.
(11) Han, S. H.; Ching, Y. C.; Rousseau, D. L. Primary Intermediate in the Reaction of Mixed-Valence Cytochrome *c* Oxidase with Oxygen. *Biochemistry* **1990**, *29*, 1380−1384.
(12) Ogura, T.; Takahashi, S.; Shinzawa-Itoh, K.; Yoshikawa, S.; Kitagawa, T. Observation of the Fe^{II}-O_2 Stretching Raman Band for Cytochrome Oxidase Compound A at Ambient Temperature. *J. Am. Chem. Soc.* **1990**, *112*, 5630−5631.
(13) Ogura, T.; Takahashi, S.; Hirota, S.; Shinzawa-Itoh, K.; Yoshikawa, S.; Appelman, E. H.; Kitagawa, T. Time-Resolved Resonance Raman Elucidation of the Pathway for Dioxygen Reduction by Cytochrome *c* Oxidase. *J. Am. Chem. Soc.* **1993**, *115*, 8527−8536.
(14) Varotsis, C.; Woodruff, W. H.; Babcock, G. T. Time-Resolved Raman Detection of ν(Fe-O) in an Early Intermediate in the Reduction of O_2 by Cytochrome-Oxidase. *J. Am. Chem. Soc.* **1989**, *111*, 6439−6440.
(15) Han Du, W.-G.; Gotz, A. W.; Noodleman, L. DFT Fe_{a3}-O/O-O Vibrational Frequency Calculations over Catalytic Reaction Cycle States in the Dinuclear Center of Cytochrome *c* Oxidase. *Inorg. Chem.* **2019**, *58*, 13933−13944.
(16) Ishigami, I.; Hikita, M.; Egawa, T.; Yeh, S. R.; Rousseau, D. L. Proton Translocation in Cytochrome *c* Oxidase: Insights from Proton Exchange Kinetics and Vibrational Spectroscopy. *Biochim. Biophys. Acta, Bioenerg.* **2015**, *1847*, 98−108.
(17) Yoshikawa, S.; Shimada, A. Reaction Mechanism of Cytochrome *c* Oxidase. *Chem. Rev.* **2015**, *115*, 1936−1989.
(18) Van Wart, H. E.; Zimmer, J. Resonance Raman Evidence for the Activation of Dioxygen in Horseradish Oxyperoxidase. *J. Biol. Chem.* **1985**, *260*, 8372−8377.
(19) Hirota, S.; Li, T. S.; Phillips, G. N.; Olson, J. S.; Mukai, M.; Kitagawa, T. Perturbation of the Fe-O_2 Bond by Nearby Residues in Heme Pocket: Observation of $\nu_{Fe\text{-}O2}$ Raman Bands for Oxymyoglobin Mutants. *J. Am. Chem. Soc.* **1996**, *118*, 7845−7846.
(20) Tsubaki, M.; Nagai, K.; Kitagawa, T. Resonance Raman Spectra of Myoglobins Reconstituted with Spirographis and Isospirographis Hemes and Iron 2,4-Diformylprotoporphyrin IX. Effect of Formyl Substitution at the Heme Periphery. *Biochemistry* **1980**, *19*, 379−385.
(21) Wikström, M. Energy-Dependent Reversal of the Cytochrome-Oxidase Reaction. *Proc. Natl. Acad. Sci. U. S. A.* **1981**, *78*, 4051−4054.
(22) Weng, L. C.; Baker, G. M. Reaction of Hydrogen-Peroxide with the Rapid Form of Resting Cytochrome-Oxidase. *Biochemistry* **1991**, *30*, 5727−5733.
(23) Morgan, J. E.; Verkhovsky, M. I.; Wikstrom, M. Observation and Assignment of Peroxy and Ferryl Intermediates in the Reduction of Dioxygen to Water by Cytochrome *c* Oxidase. *Biochemistry* **1996**, *35*, 12235−12240.
(24) Proshlyakov, D. A.; Pressler, M. A.; Babcock, G. T. Dioxygen Activation and Bond Cleavage by Mixed-Valence Cytochrome *c* Oxidase. *Proc. Natl. Acad. Sci. U. S. A.* **1998**, *95*, 8020−8025.
(25) Fabian, M.; Wong, W. W.; Gennis, R. B.; Palmer, G. Mass Spectrometric Determination of Dioxygen Bond Splitting in the "Peroxy" Intermediate of Cytochrome *c* Oxidase. *Proc. Natl. Acad. Sci. U. S. A.* **1999**, *96*, 13114−13117.
(26) Han Du, W.-G.; Götz, A. W.; Noodleman, L. A Water Dimer Shift Activates a Proton Pumping Pathway in the $\mathbf{P_R} \rightarrow \mathbf{F}$ Transition of ba_3 Cytochrome c Oxidase. *Inorg. Chem.* **2018**, *57*, 1048−1059.
(27) Siletsky, S. A.; Belevich, I.; Belevich, N. P.; Soulimane, T.; Wikstrom, M. Time-Resolved Generation of Membrane Potential by ba_3 Cytochrome *c* Oxidase from *Thermus thermophilus* Coupled to Single Electron Injection Into the **O** and $\mathbf{O_H}$ States. *Biochim. Biophys. Acta, Bioenerg.* **2017**, *1858*, 915−926.
(28) Szundi, I.; Funatogawa, C.; Fee, J. A.; Soulimane, T.; Einarsdottir, O. CO Impedes Superfast O_2 Binding in ba_3 Cytochrome Oxidase from *Thermus thermophilus*. *Proc. Natl. Acad. Sci. U. S. A.* **2010**, *107*, 21010−21015.
(29) Bloch, D.; Belevich, I.; Jasaitis, A.; Ribacka, C.; Puustinen, A.; Verkhovsky, M. I.; Wikström, M. The Catalytic Cycle of Cytochrome c Oxidase Is Not the Sum of Its Two Halves. *Proc. Natl. Acad. Sci. U. S. A.* **2004**, *101*, 529−533.
(30) Belevich, I.; Bloch, D. A.; Belevich, N.; Wikström, M.; Verkhovsky, M. I. Exploring the Proton Pump Mechanism of Cytochrome *c* Oxidase In Real Time. *Proc. Natl. Acad. Sci. U. S. A.* **2007**, *104*, 2685−2690.
(31) Siletsky, S. A.; Belevich, I.; Wikström, M.; Soulimane, T.; Verkhovsky, M. I. Time-Resolved $O_H \rightarrow E_H$ Transition of the Aberrant ba_3 Oxidase from *Thermus thermophilus*. *Biochim. Biophys. Acta, Bioenerg.* **2009**, *1787*, 201−205.
(32) Moody, A. J. 'As Prepared' Forms of Fully Oxidised Haem/Cu Terminal Oxidases. *Biochim. Biophys. Acta, Bioenerg.* **1996**, *1276*, 6−20.
(33) Ostermeier, C.; Harrenga, A.; Ermler, U.; Michel, H. Structure at 2.7 Å Resolution of the *Paracoccus denitrificans* Two-Subunit Cytochrome *c* Oxidase Complexed with an Antibody F_V Fragment. *Proc. Natl. Acad. Sci. U. S. A.* **1997**, *94*, 10547−10553.
(34) Qin, L.; Hiser, C.; Mulichak, A.; Garavito, R. M.; Ferguson-Miller, S. Identification of Conserved Lipid/Detergent-Binding Sites in A High-Resolution Structure of the Membrane Protein Cytochrome *c* Oxidase. *Proc. Natl. Acad. Sci. U. S. A.* **2006**, *103*, 16117−16122.

https://dx.doi.org/10.1021/acs.inorgchem.0c00724
Inorg. Chem. 2020, 59, 8906−8915

(35) Koepke, J.; Olkhova, E.; Angerer, H.; Muller, H.; Peng, G. H.; Michel, H. High Resolution Crystal Structure of *Paracoccus denitrificans* Cytochrome *c* Oxidase: New Insights into the Active Site and the Proton Transfer Pathways. *Biochim. Biophys. Acta, Bioenerg.* **2009**, *1787*, 635−645.
(36) Aoyama, H.; Muramoto, K.; Shinzawa-Itoh, K.; Hirata, K.; Yamashita, E.; Tsukihara, T.; Ogura, T.; Yoshikawa, S. A Peroxide Bridge Between Fe and Cu Ions in the O_2 Reduction Site of Fully Oxidized Cytochrome *c* Oxidase Could Suppress the Proton Pump. *Proc. Natl. Acad. Sci. U. S. A.* **2009**, *106*, 2165−2169.
(37) Tiefenbrunn, T.; Liu, W.; Chen, Y.; Katritch, V.; Stout, C. D.; Fee, J. A.; Cherezov, V. High Resolution Structure of the ba_3 Cytochrome *c* Oxidase from *Thermus thermophilus* in a Lipidic Environment. *PLoS One* **2011**, *6*, e22348.
(38) Hirata, K.; Shinzawa-Itoh, K.; Yano, N.; Takemura, S.; Kato, K.; Hatanaka, M.; Muramoto, K.; Kawahara, T.; Tsukihara, T.; Yamashita, E.; Tono, K.; Ueno, G.; Hikima, T.; Murakami, H.; Inubushi, Y.; Yabashi, M.; Ishikawa, T.; Yamamoto, M.; Ogura, T.; Sugimoto, H.; Shen, J. R.; Yoshikawa, S.; Ago, H. Determination of Damage-Free Crystal Structure of An X-Ray-Sensitive Protein Using An XFEL. *Nat. Methods* **2014**, *11*, 734−U174.
(39) Andersson, R.; Safari, C.; Dods, R.; Nango, E.; Tanaka, R.; Yamashita, A.; Nakane, T.; Tono, K.; Joti, Y.; Bath, P.; Dunevall, E.; Bosman, R.; Nureki, O.; Iwata, S.; Neutze, R.; Branden, G. Serial Femtosecond Crystallography Structure of Cytochrome *c* Oxidase at Room Temperature. *Sci. Rep.* **2017**, *7*, 4518.
(40) Ueno, G.; Shimada, A.; Yamashita, E.; Hasegawa, K.; Kumasaka, T.; Shinzawa-Itoh, K.; Yoshikawa, S.; Tsukihara, T.; Yamamoto, M. Low-Dose X-Ray Structure Analysis of Cytochrome *c* Oxidase Utilizing High-Energy X-Rays. *J. Synchrotron Radiat.* **2019**, *26*, 912−921.
(41) Kaila, V. R. I.; Oksanen, E.; Goldman, A.; Bloch, D. A.; Verkhovsky, M. I.; Sundholm, D.; Wikström, M. A Combined Quantum Chemical and Crystallographic Study on the Oxidized Binuclear Center of Cytochrome *c* Oxidase. *Biochim. Biophys. Acta, Bioenerg.* **2011**, *1807*, 769−778.
(42) Han Du, W.-G.; Noodleman, L. Density Functional Study for the Bridged Dinuclear Center Based on a High-Resolution X-Ray Crystal Structure of ba_3 Cytochrome *c* Oxidase from *Thermus thermophilus*. *Inorg. Chem.* **2013**, *52*, 14072−14088.
(43) Siletskiy, S.; Soulimane, T.; Azarkina, N.; Vygodina, T. V.; Buse, G.; Kaulen, A.; Konstantinov, A. Time-Resolved Generation of A Membrane Potential by ba_3 Cytochrome *c* Oxidase from *Thermus thermophilus*. Evidence for Reduction-Induced Opening of the Binuclear Center. *FEBS Lett.* **1999**, *457*, 98−102.
(44) Siletsky, S. A. Steps of the Coupled Charge Translocation in the Catalytic Cycle of Cytochrome *c* Oxidase. *Front. Biosci., Landmark Ed.* **2013**, *18*, 36−57.
(45) Grimme, S.; Ehrlich, S.; Goerigk, L. Effect of the Damping Function in Dispersion Corrected Density Functional Theory. *J. Comput. Chem.* **2011**, *32*, 1456−1465.
(46) *ADF, Amsterdam Density Functional Software*; SCM, Theoretical Chemistry, Vrije Universiteit: Amsterdam, The Netherlands; http://www.scm.com.
(47) te Velde, G.; Bickelhaupt, F. M.; Baerends, E. J.; Guerra, C. F.; Van Gisbergen, S. J. A.; Snijders, J. G.; Ziegler, T. Chemistry with ADF. *J. Comput. Chem.* **2001**, *22*, 931−967.
(48) Guerra, C. F.; Visser, O.; Snijders, J. G.; te Velde, G.; Baerends, E. J., Parallelisation of the Amsterdam Density Functional Program. In *Methods and techniques for computational chemistry*; Clementi, E., Corongiu, C., Eds.; STEF: Cagliari, 1995; pp 303−395.
(49) Goerigk, L.; Hansen, A.; Bauer, C.; Ehrlich, S.; Najibi, A.; Grimme, S. A Look at the Density Functional Theory Zoo with the Advanced GMTKN55 Database for General Main Group Thermochemistry, Kinetics and Noncovalent Interactions. *Phys. Chem. Chem. Phys.* **2017**, *19*, 32184−32215.
(50) Noodleman, L. Valence Bond Description of Anti-Ferromagnetic Coupling in Transition-Metal Dimers. *J. Chem. Phys.* **1981**, *74*, 5737−5743.
(51) Noodleman, L.; Case, D. A. Density-Functional Theory of Spin Polarization and Spin Coupling in Iron-Sulfur Clusters. *Adv. Adv. Inorg. Chem.* **1992**, *38*, 423−470.
(52) Noodleman, L.; Lovell, T.; Han, W.-G.; Liu, T.; Torres, R. A.; Himo, F. Density Functional Theory. In *Comprehensive Coordination Chemistry II, From Biology to Nanotechnology*; Lever, A. B., Ed.; Elsevier: 2003; Vol. *2*, pp 491−510.
(53) Klamt, A.; Schüürmann, G. COSMO - A New Approach to Dielectric Screening in Solvents with Explicit Expressions for the Screening Energy and Its Gradient. *J. Chem. Soc., Perkin Trans. 2* **1993**, 799−805.
(54) Klamt, A. Conductor-Like Screening Model for Real Solvents - A New Approach to the Quantitative Calculation of Solvation Phenomena. *J. Phys. Chem.* **1995**, *99*, 2224−2235.
(55) Klamt, A.; Jonas, V. Treatment of the Outlying Charge in Continuum Solvation Models. *J. Chem. Phys.* **1996**, *105*, 9972−9981.
(56) Pye, C. C.; Ziegler, T. An Implementation of the Conductor-Like Screening Model of Solvation within the Amsterdam Density Functional Package. *Theor. Chem. Acc.* **1999**, *101*, 396−408.
(57) Han, S.; Takahashi, S.; Rousseau, D. L. Time Dependence of the Catalytic Intermediates in Cytochrome *c* Oxidase. *J. Biol. Chem.* **2000**, *275*, 1910−1919.
(58) Zimmermann, B. H.; Nitsche, C. I.; Fee, J. A.; Rusnak, F.; Munck, E. Properties of A Copper-Containing Cytochrome ba_3: A Second Terminal Oxidase from the Extreme Thermophile *Thermus thermophilus*. *Proc. Natl. Acad. Sci. U. S. A.* **1988**, *85*, 5779−5783.
(59) Rusnak, F. M.; Munck, E.; Nitsche, C. I.; Zimmermann, B. H.; Fee, J. A. Evidence for Structural Heterogeneities and A Study of Exchange Coupling. Mössbauer Studies of Cytochrome c_1aa_3 from *Thermus thermophilus*. *J. Biol. Chem.* **1987**, *262*, 16328−16332.
(60) Noodleman, L.; Han Du, W.-G.; Fee, J. A.; Götz, A. W.; Walker, R. C. Linking Chemical Electron-Proton Transfer to Proton Pumping in Cytochrome *c* Oxidase: Broken-Symmetry DFT Exploration of Intermediates along the Catalytic Reaction Pathway of the Iron-Copper Dinuclear Complex. *Inorg. Chem.* **2014**, *53*, 6458−6472.
(61) Han Du, W.-G.; Noodleman, L. Broken Symmetry DFT Calculations/Analysis for Oxidized and Reduced Dinuclear Center in Cytochrome *c* Oxidase: Relating Structures, Protonation States, Energies, and Mössbauer Properties in ba_3 *Thermus thermophilus*. *Inorg. Chem.* **2015**, *54*, 7272−7290.
(62) Tissandier, M. D.; Cowen, K. A.; Feng, W. Y.; Gundlach, E.; Cohen, M. H.; Earhart, A. D.; Coe, J. V.; Tuttle, T. R. The proton's absolute aqueous enthalpy and Gibbs free energy of solvation from cluster-ion solvation data. *J. Phys. Chem. A* **1998**, *102*, 7787−7794.
(63) Truhlar, D. G.; Cramer, C. J.; Lewis, A.; Bumpus, J. A. Molecular modeling of environmentally important processes: Reduction potentials. *J. Chem. Educ.* **2004**, *81*, 596−604.
(64) Truhlar, D. G.; Cramer, C. J.; Lewis, A.; Bumpus, J. A. Molecular modeling of environmentally important processes: Reduction potentials (vol 81, pg 596, 2004). *J. Chem. Educ.* **2007**, *84*, 934.
(65) Marenich, A. V.; Ho, J. M.; Coote, M. L.; Cramer, C. J.; Truhlar, D. G. Computational electrochemistry: prediction of liquid-phase reduction potentials. *Phys. Chem. Chem. Phys.* **2014**, *16*, 15068−15106.
(66) Tawa, G. J.; Topol, I. A.; Burt, S. K.; Caldwell, R. A.; Rashin, A. A. Calculation of the aqueous solvation free energy of the proton. *J. Chem. Phys.* **1998**, *109*, 4852−4863.

https://dx.doi.org/10.1021/acs.inorgchem.0c00724
Inorg. Chem. 2020, 59, 8906−8915